Chaos
An Interdisciplinary Journal of Nonlinear Science
AIP Publishing

Fast-slow analysis and bifurcations in the generation of the early afterdepolarization phenomenon in a realistic mathematical human ventricular myocyte model

Hiroyuki Kitajima,[1] Toru Yazawa,[1] and Roberto Barrio[2]
[1)]*Faculty of Engineering and Design, Kagawa University, 2217-20 Hayashi, Takamatsu, Kagawa, 761-0396 Japan*
[2)]*Departamento de Matemática Aplicada and IUMA. Computational Dynamics group. Universidad de Zaragoza. E-50009. Spain.*

(*Electronic mail: rbarrio@unizar.es)

(*Electronic mail: tryazawa@gmail.com)

(*Electronic mail: kitajima.hiroyuki@kagawa-u.ac.jp)

(Dated: November 1, 2024)

Early afterdepolarizations (EADs) are spontaneous oscillations in membrane potential that occur during the repolarization phase of the action potential. EADs can trigger ventricular arrhythmias, such as Torsades de Pointes, in patients with long QT syndromes. Understanding the theoretical mechanisms behind EAD generation and developing strategies to suppress them are crucial. In this study, we employed bifurcation analysis along with a new fast-slow decomposition method on the O'Hara model of human ventricular myocytes. Our goal was to examine how the calcium ion concentration in the network sarcoplasmic reticulum (NSR) influences the generation of EADs in the context of reduced rapid delayed rectifier K^+ current. Our findings identified nine distinct EAD states that coexist and can be controlled by slight adjustments to the NSR calcium ion concentration at a single time point.

Keywords: Early afterdepolarization, bifurcations, mathematical calcium ion concentration, mathematical ventricular cardiomyocyte model, network sarcoplasmic reticulum

In diseases such as heart failure, early afterdepolarizations (EADs) are recognized as a significant cause of lethal ventricular arrhythmias. Despite extensive research, a deeper understanding of the mechanisms underlying EAD generation is still needed. Realistic computational models of cardiac electrical activity have made substantial contributions to studying these phenomena. While highly detailed models, with numerous state variables, provide a more accurate representation of experimental observations and offer valuable biophysical insights, they tend to be too complex for in-depth analysis. In this study, we investigated the generation of EADs and repolarization failure (persistent EAD oscillations) in the O'Hara model by analyzing their dependence on various parameters. We parameterized $[Ca]_{nsr}$, the concentration of calcium ions in the network sarcoplasmic reticulum (NSR), which is the slowest variable in the system. This allowed us to apply bifurcation analysis and utilize a fast-slow decomposition of the original model, providing a dynamical systems explanation for the different observed dynamics. Through theoretical analysis, we explored the influence of NSR calcium concentration and identified that the pathological states in the original system could be explained by the bifurcations in the parameterized model. We demonstrated the coexistence of multiple EADs and repolarization failure states, showing that these anomalous states could be controlled by adjusting the NSR calcium concentration at a single time point.

I. INTRODUCTION

Early afterdepolarizations (EADs) are spontaneous oscillations in membrane potential occurring during the repolarizing phase of the action potential. EADs can trigger ventricular arrhythmias, such as Torsades de Pointes[1–3], particularly in patients with long QT syndromes, which may lead to sudden death due to ventricular fibrillation. This study focuses on the theoretical analysis of EADs. Typically, EAD occurrence is associated with an increase in the L-type calcium current or a decrease in potassium current[1,4–17].

Investigating mathematical cardiac models is crucial for understanding the mechanisms behind EAD generation. Low-dimensional models have been analyzed using bifurcation theory and time-scale separation, or fast-slow analysis[18–21]. These studies have shown that EADs can result from various dynamical systems phenomena, including Hopf and homoclinic bifurcations in mathematical models[22], which have also been observed in experiments[23]. Other mechanisms include folded node singularities of the slow flow[19,24,25], canards[25–28], period-doubling bifurcation cascades[29], and delayed subcritical Hopf bifurcations[30]. Landaw and Qu developed an iterated map model that showed long-periodic solutions with alternating EAD and no-EAD episodes, caused by a Hopf bifurcation in the discrete-time model[31]. While these low-dimensional models help clarify the mathematical mechanisms of EAD generation from a dynamical systems perspective, high-dimensional models incorporating a wide range of ionic currents are needed to explore the biological mechanisms.

Previous studies using detailed mathematical models have shown that EAD generation is associated with slow variables

such as intracellular sodium ion concentration, as demonstrated by Krogh-Madsen and Christini[32]. Tsumoto et al. studied the multi-stability of transient EADs[33] (short term EAD orbits before converging to another state), and Xie et al. revealed that repeating EAD and no-EAD states exhibit hysteresis characteristics[34]. These phenomena's dependence on system parameters has been examined through bifurcation analysis[35]. Different models feature other slow variables, such as intracellular potassium and calcium ion concentrations. The intracellular potassium concentration, for example, may drift over time without reaching a steady state[36], so it is typically fixed. The number of EADs has been linked to calcium ion concentrations in various compartments, including the sarcoplasmic reticulum (SR)[37,38], intracellular compartment[1], junctional sarcoplasmic reticulum (JSR)[9,39], cytoplasm[2], and network sarcoplasmic reticulum (NSR)[40]. However, these studies primarily focused on observations of these phenomena.

In this study, we aimed to investigate the effects of calcium ion concentrations on EAD generation —specifically the number of EADs— using bifurcation theory. We sought to provide a theoretical explanation for the observed phenomena. Previous studies[41,42] have shown that bifurcations in the Luo-Rudy 3D model and the 27D model by Sato et al. lead to the creation of the first EAD, but a more detailed bifurcation analysis of the 27D model is required. Thus, the main objective of this article is to conduct a comprehensive bifurcation analysis in a realistic cardiomyocyte model.

Our analysis revealed that a higher concentration of calcium ions in the NSR promotes the formation of more EADs or small oscillations. We demonstrated the coexistence of multiple EAD states and showed that these states could be controlled —transitioning to fewer EADs— by adjusting the NSR calcium ion concentration. By examining ionic currents during this transition, we found that increasing the inward rectifier potassium current suppressed EADs, while increasing the outward calcium current through the L-type channel promoted them. Additionally, we clarified that the ultra-long action potential duration (APD) and related fibrillation observed in experiments[39,43–47] and simulations[4,39,48,49] were driven by elevated NSR calcium concentrations. These findings may provide new theoretical insights or practical approaches for controlling EAD generation.

This article is structured as follows: Section II provides a brief description of the O'Hara mathematical model for the human ventricular myocyte. In Section III, we introduce the parameterized model and analyze its dynamics. Section IV compares both models using a fast-slow decomposition approach. In Section V, we propose a simple control mechanism to mitigate EADs. Finally, Section VI offers a discussion and our conclusions.

II. O'HARA HUMAN VENTRICULAR CARDIOMYOCYTE MODEL

The O'Hara model is a realistic mathematical model that describes the electrophysiological mechanisms of human ventricular myocytes[50]. The membrane potential is governed by

$$C\frac{dV}{dt} = -(I_{\mathrm{Na}} + I_{\mathrm{NaK}} + I_{\mathrm{CaL}} + I_{\mathrm{CaNa}} + I_{\mathrm{CaK}} + I_{\mathrm{NaCa}_i} + I_{\mathrm{NaCa}_{ss}} + I_{\mathrm{NaCa}} + I_{\mathrm{Ks}} + I_{\mathrm{Kr}} + I_{\mathrm{K1}} + I_{to} + I_{\mathrm{Nab}} + I_{\mathrm{Cab}} + I_{\mathrm{Kb}} + I_{\mathrm{pCa}} + I_{\mathrm{sti}}), \quad (1)$$

where V (mV) represents the membrane potential, C (μF) is the cell membrane capacitance, and I_j (μA/μF) represents the ionic currents, excluding the stimulus pulse current I_{sti}, which has an amplitude of 60 (μA/μF), a duration of 1 (ms), and a period of 2000 (ms). Table 1[50] provides a list of all ionic currents included in this model.

Some ionic currents have the following form

$$I_j = g_j \cdot y_{g1}^{m_1} y_{g2}^{m_2} y_{g3}^{m_3} \cdot (V - E_j),$$

where g_j is the maximum conductance and E_j is the reversal potentials for ion j. The gating variables y_g are given by

$$\frac{dy_g}{dt} = \frac{y_{\infty,g} - y_g}{\tau_{y_g}}$$

where τ_{y_g} and $y_{\infty,g}$ are time constant and the value of y_g in the steady state, respectively. The O'Hara model includes 29 gating variables and is described by a system of 41-dimensional ordinary differential equations (see Ref. 50 for the full model equations). We fixed the sodium and potassium ion concentrations at 8.0 (mM) and 140.0 (mM), respectively, reducing the model to 37 dimensions. It is known that EADs can be induced by blocking I_{Kr} during slow pacing, so we selected the I_{Kr} multiplier as a control parameter. The typical maximum conductance of I_{Kr} is 0.0368, and we varied g_{Kr} (0 to 100%) as the control parameter. All other parameters were set to their normal values[50].

Table I. Ionic currents in O'Hara model

Abbreviation	Ionic current
I_{Na}	Na^+ current
I_{NaK}	Na^+/K^+ ATPase current
I_{CaL}	Ca^{2+} current through the L-type Ca^{2+} channel
I_{CaNa}	Na^+ current through the L-type Ca^{2+} channel
I_{CaK}	K^+ current through the L-type Ca^{2+} channel
I_{NaCa_i}	myoplasmic component of Na^+/Ca^{2+} exchange current
$I_{\mathrm{NaCa}_{ss}}$	subspace component of Na^+/Ca^{2+} exchange current
I_{NaCa}	total Na^+/Ca^{2+} exchange current
I_{Ks}	slow delayed rectifier K^+ current
I_{Kr}	rapid delayed rectifier K^+ current
I_{K1}	inward rectifier K^+ current
I_{to}	transient outward K^+ current
I_{Nab}	Na^+ background current
I_{Cab}	Ca^{2+} background current
I_{Kb}	K^+ background current
I_{pCa}	sarcolemmal Ca^{2+} pump current

It is worth noting that while more detailed models exist in the literature, the O'Hara model offers valuable insights into the realistic dynamics of human ventricular myocytes.

In this study, all numerical continuation analyses of bifurcations, both for equilibria and periodic orbits, were conducted using specialized software described in Ref. 51. This software is particularly suited for continuation studies in high-dimensional systems. It employs standard continuation techniques and also facilitates stability analysis of equilibria and periodic orbits through the calculation of eigenvalues of the Jacobian matrix and the Floquet multipliers, respectively.

III. PARAMETERIZED MODEL AND DYNAMICS

To investigate the mechanisms behind the generation of EADs in the O'Hara model, we initially attempted to apply the same approach used in recent studies on low-dimensional models, which employed a fast-slow decomposition of the system's dynamics. In these studies, various 3D or 4D cardiomyocyte models were examined[18–21,24–28], where slow variables were easily identifiable.

Fast-slow decomposition has proven to be an effective method for studying the bifurcation origins of EADs in low-dimensional systems. For example, Ref. 41 established a link between numerical simulations in a realistic model and the fast-slow decomposition of a low-dimensional model (the 3D Luo-Rudy model). However, it remains unclear whether this decomposition remains valid in a realistic high-dimensional model, as obtaining such a decomposition presents significant computational challenges. In this paper, we aim to address this issue by investigating whether the assumptions made in the literature hold in a realistic model. Our focus is on developing an approach that allows us to perform a fast-slow decomposition in a highly complex system.

Since we are dealing with a high-dimensional problem, our approach differs from those used in previous studies[19,24–28] on low-dimensional models with small explicit parameters. We begin by identifying the slowest variable in the absence of a stimulus, then fix that variable to create two models: the original model and a modified version with the slowest variable held constant (the limiting case). The primary reasoning is that the stimulus induces rapid depolarization, after which the system's dynamics are governed by the behavior without the stimulus. This observation allows us to approximate the fast subsystem by treating the slowest variable as constant and removing the stimulus to focus on the model's internal dynamics. Given the high dimensionality of the reduced model (36 variables), it is crucial to examine its bifurcations and understand how they organize the dynamics of the original problem. This approach mirrors those used in low-dimensional models[19,24–28].

As a first step, we examined the convergence speed of all state variables in the O'Hara model without a stimulus ($I_{\text{sti}} = 0$). We present the results for the two slowest variables, $[\text{Ca}]_{\text{nsr}}$ (calcium ion concentration in the network sarcoplasmic reticulum) and $[\text{Ca}]_{\text{jsr}}$ (calcium ion concentration in the junctional sarcoplasmic reticulum), in Fig. 1(a). The vertical axis shows the difference between the previous time point ($[\text{Ca}]^{i-1}_{\{\text{n,j}\}\text{sr}}$) and the current time point ($[\text{Ca}]^{i}_{\{\text{n,j}\}\text{sr}}$) during numerical integration with a fixed step size of 1/256 ms. Note that all state variables converge to an equilibrium point for the chosen parameter values, causing these differences to approach zero.

We found that $[\text{Ca}]_{\text{nsr}}$ and $[\text{Ca}]_{\text{jsr}}$ exhibited the slowest dynamics. Therefore, to determine which variable to fix, we considered two cases, fixing either $[\text{Ca}]_{\text{nsr}}$ or $[\text{Ca}]_{\text{jsr}}$, and checked the convergence speed in each case. Figure 1(b) shows that the speed was significantly improved when $[\text{Ca}]_{\text{nsr}}$ was fixed, due to the fact that the slow dynamics of $[\text{Ca}]_{\text{nsr}}$ affect the convergence speed of $[\text{Ca}]_{\text{jsr}}$. As a result, we created a new system, referred to as the $[\text{Ca}]_{\text{nsr}}$-*parameterized system*, where $[\text{Ca}]_{\text{nsr}}$ is treated as a parameter and $I_{\text{sti}} = 0$ (no stimulus).

As discussed, this reduced model will serve as the fast subsystem, with the fixed variable $[\text{Ca}]_{\text{nsr}}$ acting as a bifurcation parameter to study the fast-slow decomposition.

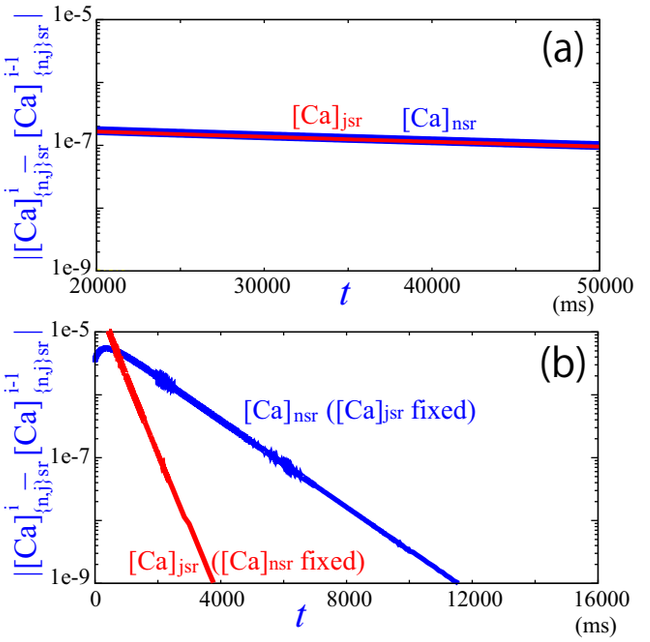

Figure 1. Convergence of state variables to equilibrium point at $g_{\text{Kr}} = 1.0$. (a) Top two slowest variables in original system. (b) Slowest state variable in $[\text{Ca}]_{\text{nsr}}$-parameterized system and in $[\text{Ca}]_{\text{jsr}}$-parameterized system.

Once we derive a slightly simplified model, the $[\text{Ca}]_{\text{nsr}}$-parameterized system, we can apply bifurcation analysis techniques using the methods and software outlined in Ref. 51. Despite the fact that this simplified model still comprises 36 variables, making it highly dimensional and complex, it can be viewed as the fast subsystem of the original model, allowing for comparison between the two systems through standard fast-slow analysis.

In Fig. 2, we show a subcritical Hopf bifurcation curve on the parameter plane of a specific equilibrium. We also identify the main bifurcations of the unstable limit cycles that arise from this Hopf bifurcation. Firstly, these cycles undergo a *Fold* bifurcation, giving rise to stable limit cycles. Subse-

quently, they experience a sequence of *period-doubling* (PD) bifurcations. Notably, a large region of the parameter plane contains at least one stable equilibrium, while in some areas, stable and unstable limit cycles coexist.

The stable equilibrium point (approximately at $V = -12$ (mV)) is present throughout all shaded regions following the subcritical Hopf bifurcation. Between the Hopf and Fold bifurcations, an unstable limit cycle exists, and after the Fold bifurcation, a small-amplitude stable limit cycle appears and exists in the region between Fold and period-doubling (PD) bifurcations, coexisting with the unstable limit cycle. Following the period-doubling bifurcation, additional period-doublings occur, leading to a cascade of bifurcations and chaotic dynamics. More details on these bifurcations are discussed in the following section. We emphasize that this description pertains to the dynamics of the parameterized model, where $[\mathrm{Ca}]_{\mathrm{nsr}}$ is fixed and no external stimulus is applied.

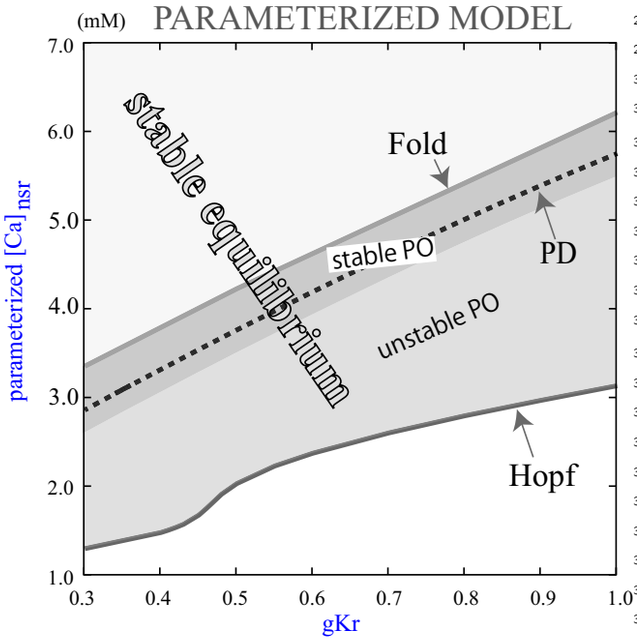

Figure 2. Two-parameter bifurcation diagram (g_{Kr}, $[\mathrm{Ca}]_{\mathrm{nsr}}$) in the $[\mathrm{Ca}]_{\mathrm{nsr}}$-parameterized system. Hopf bifurcation of an equilibrium point, and period-doubling (PD) and Fold bifurcations of limit cycles are present. A stable equilibrium point is observed in a large region, and stable and unstable limit cycles created at the Hopf bifurcation are observed in dark gray and light gray regions, respectively.

The key question is: what are the dynamics of the original O'Hara model, and how do they relate to those observed in the parameterized model? Figure 3(a) presents a one-parameter bifurcation diagram for the original system, where $[\mathrm{Ca}]_{\mathrm{nsr}}$ is now a variable of the model. The vertical axis shows the $[\mathrm{Ca}]_{\mathrm{nsr}}$ values at intervals of 2000 (ms) (i.e. Poincaré mapping) for different steady states, such as repolarization failure, EADs, and normal behavior. Additionally, it highlights the region where transient EADs occur —EADs that disappear after a convergence process— when g_{Kr} exceeds 0.4.

The figure also includes the bifurcation sets calculated for the $[\mathrm{Ca}]_{\mathrm{nsr}}$-parameterized system, previously presented in Fig. 2. Notably, the region containing transient EADs, repolarization failure (persistent EAD oscillations), and EADs lies within the region of limit cycles in the parameterized system. Furthermore, the upper boundary of orbits with EADs is precisely defined by the period-doubling bifurcation curve of the limit cycles in the parameterized model, while repolarization failure occurs within the stable limit cycle region, between the Fold and period-doubling bifurcation curves.

These observations are important for two key reasons. First, the parameterized system approach allows us to clearly delineate the regions of interest, as all orbits with EADs and repolarization failure are accurately bounded by the bifurcations in the parameterized model. Moreover, this approach enables the use of fast-slow decomposition techniques, as detailed in the next section. Second, it underscores the significant connection between the generation of EADs and the prior development of alternans, in this case through period-doubling bifurcations. This relationship has been demonstrated in both experiments and numerical simulations[41,52], but explicit bifurcation analysis in high-dimensional models has been lacking, despite being conjectured in both low- and high-dimensional models[42].

An enlarged and superimposed diagram of a section from Fig. 3(a) is shown in Fig. 3(b). Within a narrow parameter range of g_{Kr}, we observe multiple stable states, including repolarization failure, 16 types of EADs, and normal states. The stable repolarization failure in the original system occurs within the region where stable limit cycles are found in the $[\mathrm{Ca}]_{\mathrm{nsr}}$-parameterized system.

In this context, the notation m^k–n^s represents sequences of k successive m EADs followed by s successive n EADs, where m and n indicate the number of EADs within a 2000 (ms) period (one action potential). In our simulations, up to ten states were found to coexist simultaneously. It is worth noting that detecting coexisting states in such a high-dimensional system is challenging due to their strong dependence on initial conditions and the complexity of the initial condition space. Our approach involved using a large initial value of $[\mathrm{Ca}]_{\mathrm{nsr}}$ (since higher $[\mathrm{Ca}]_{\mathrm{nsr}}$ was found to promote more EADs, as shown later) at a fixed g_{Kr}, and we confirmed convergence to a specific state —whether it be repolarization failure, EADs, or normal. Once an attractor was found for a given g_{Kr}, we used it as the initial condition for a slightly adjusted g_{Kr}. Repeating this process allowed us to discover a wide range of stable states in the desired parameter region, and we estimate that, in most cases, we were able to capture all coexisting attractors. In Fig. 3(b), we observe that the region of unstable limit cycles in the parameterized system encompasses all orbits with EADs, while repolarization failure occurs within the stable limit cycle region. Fast-slow analysis will provide further insight into this phenomenon.

Is there any ordering in the orbits with EADs? The answer is, of course, yes. In Fig. 3(b), we highlight several pathways among the EAD orbits, indicated by arrows and circles. For example, the main route leading to repolarization failure is on the left side, progressing from a normal beat (denoted by the 0 pattern) to infinity, following the sequence ∞ via $0 \to 0^m\text{–}1 \to 0\text{–}1 \to 0\text{–}2 \to 0\text{–}n \to \infty$. The corresponding waveforms of

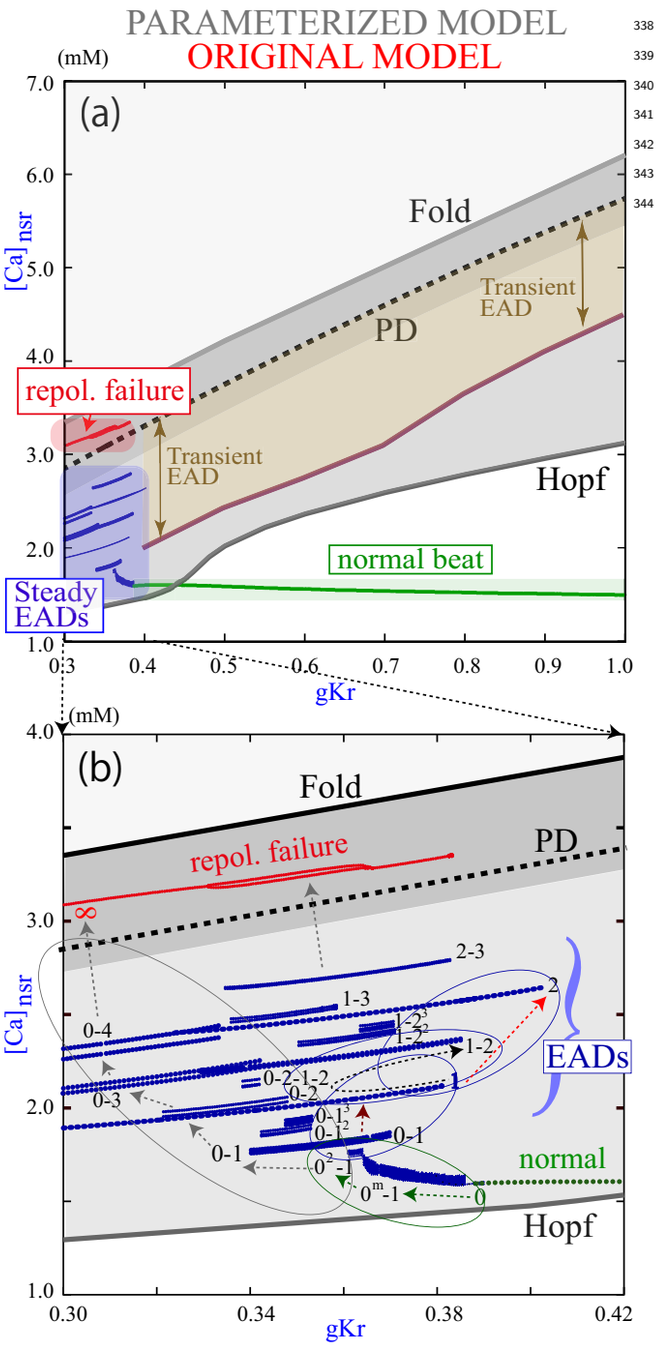

Figure 3. (a) One-parameter bifurcation diagram in the original system. The bifurcations curves from the parameterized system (Fig. 2) are shown for comparison. The values of $[Ca]_{nsr}$ every 2000 (ms), i.e. Poincaré mapping, show EADs (blue), repolarization failure (red), and normal (green) behavior. Transient EADs are also observed. The upper limit of its existence corresponds to a period-doubling bifurcation curve (dotted curve) from the parameterized system. (b) A magnification of the EAD-repolarization failure region. 16 kinds of EADs, repolarization failure, and normal states coexist in the original system. Several transition routes between different EAD patterns are highlighted (see text for details).

the membrane potentials for some of these attractors, depicted in Fig. 3(b), are shown in Figs. 4(a) to (e). Additionally, there are intermediate symbolic dynamics, such as the route from 0 to 1 via $0\text{–}1^l$, from 1 to 2 via $1\text{–}2^l$. More complex cases also arise, such as transitions of the form 0–2–1–2, and other variations. Below, in Fig. 5, we present examples of patterns with these more intricate symbolic representations.

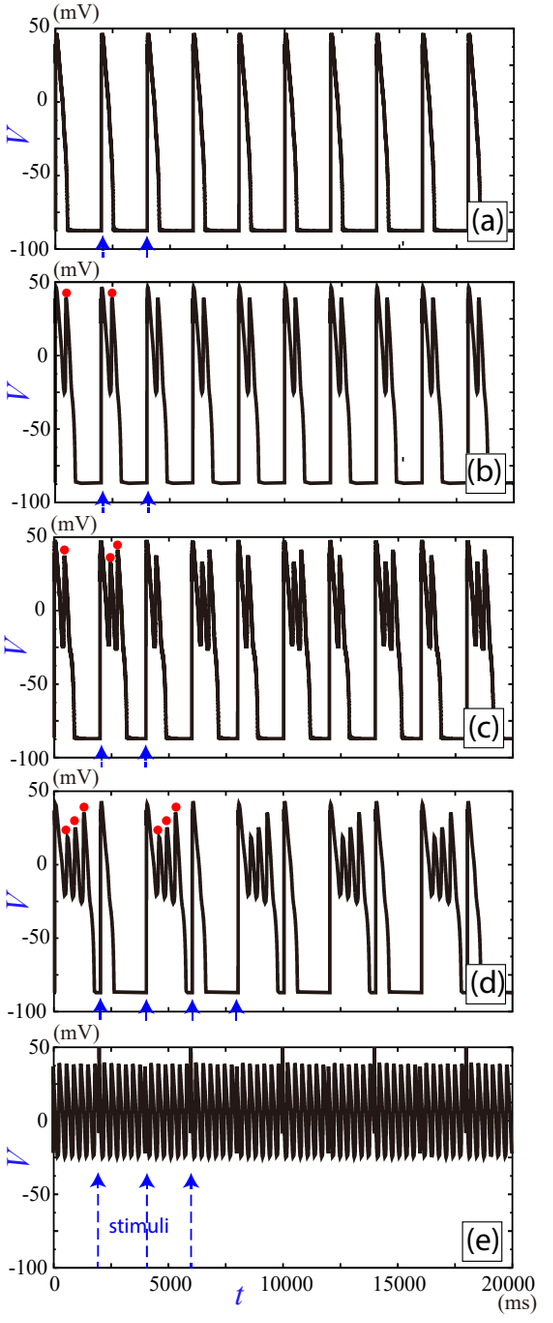

Figure 4. Membrane potential waveforms. EADs are indicated by red dots at the onset to distinguish them from the stimuli. (a) Normal at $g_{Kr} = 0.42$.(b) 1 EAD at $g_{Kr} = 0.36$. (c) 1–2 EADs at $g_{Kr} = 0.36$. (d) 0–3 EADs at $g_{Kr} = 0.32$. (e) Repolarization failure (persistent EAD oscillations) at $g_{Kr} = 0.36$.

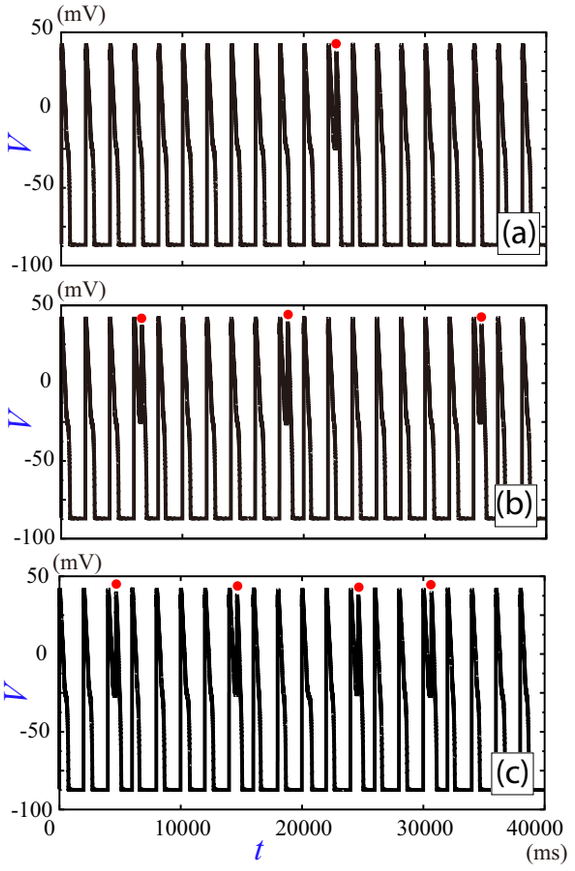

Figure 5. Complex membrane potential waveforms with several EAD rates. (a) EAD pattern 0^{16}–1 with rate 0.058 at $g_{Kr} = 0.38$. (b) EAD pattern 0^7–1–0^5–1 with rate 0.14 at $g_{Kr} = 0.37$. (c) EAD pattern $(0^4–1)^2$–0^2–1 with rate 0.23 at $g_{Kr} = 0.365$.

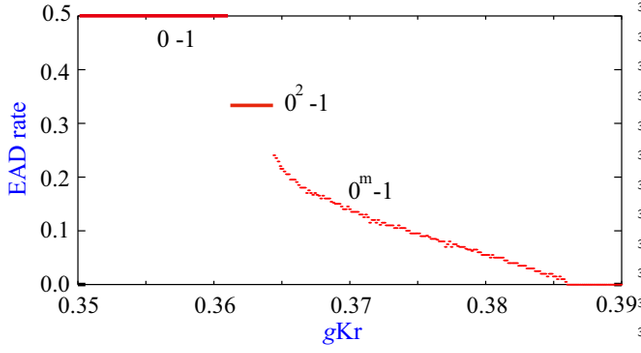

Figure 6. EAD rate calculated after $n = 1000$ APs (EAD rate = number EADs/number APs).

To explain the transition from the 0^m-1 state to 0–1 state in Fig. 3(b), we defined the EAD rate as the number of EADs divided by the number of action potentials (considering $n = 1000$ action potentials). Figure 6 illustrates the EAD rate between $g_{Kr} = 0.35$ and 0.39. In the 0^m–1 state from Fig. 3(b), we observe a transition from an EAD rate of 0 (normal) to 0.23, revealing the so-called cardiac devil's staircase[41,42]. This staircase curve reflects how the EAD rate increases step by step. The mechanism driving the discontinuous transitions from 0^m–1 to 0^2–1, and from 0^2–1 to 0–1, is based on the presence of intermediate complex patterns that facilitate the switch between different states. For a detailed explanation of this transition in the devil's staircase for another cardiomyocyte model, see Ref. 41. More complex membrane potential waveforms with varying EAD ratios are presented in Fig. 5.

We observe that intermediate complex patterns can coexist, leading to transient or stable chaotic dynamics over a narrow range of parameters. By using the EAD rate, we can more easily classify these patterns. For instance, the 0–4, 1–3, and 2 EAD patterns in Fig. 3(b) all share the same EAD rate of 2 and are nearly aligned along the same line. This highlights the intricate structure of the periodic orbits with EADs and, more importantly, shows that they are confined to specific regions in the one-parameter diagram. The different coexisting periodic orbits occupy distinct ranges of the $[Ca]_{nsr}$ variable.

IV. PARAMETERIZED AND ORIGINAL MODEL: FAST-SLOW DECOMPOSITION

In Fig. 3, we observed how the bifurcations in the parameterized model delineate certain dynamics of the original model. This makes it worthwhile to explore the spatial position of the orbits in the original system relative to the parameterized model in greater detail. To do so, we computed various bifurcation sets for the $[Ca]_{nsr}$-parameterized model at a fixed value of g_{Kr}. We then generated one-parameter bifurcation diagrams, using the voltage variable V as the vertical axis, and superimposed some of the orbits from the original model onto these diagrams.

In Fig. 7, we present a one-parameter bifurcation diagram for the parameterized model in the ($[Ca]_{nsr}$, V) plane for $g_{Kr} = 0.38$, highlighting the manifold of equilibria in green and marking the subcritical Hopf bifurcation point. The heavy black curves represent the limit cycles, with the maximum and minimum membrane potential V values of the cycles shown. Solid curves indicate stable invariants, while dashed curves indicate unstable ones. The manifold of equilibria forms the slow manifold of the fast subsystem of the original model, which is represented by the parameterized model (with the slowest variable fixed). The fast-manifold of the fast subsystem is made up of the limit cycles of the parameterized system. This fast-manifold takes on a "Mexican hat" shape, consisting of both unstable and stable sheets (we provide a schematic of this surface configuration). The stable branches of the limit cycles undergo period-doubling bifurcations, resulting in a period-doubling cascade that leads to chaotic behavior. It is important to note that this chaotic behavior forms the core mechanism behind the generation of highly complex dynamics in the original model.

Figures 8(a) and 8(b) show one-parameter bifurcation diagrams for the $[Ca]_{nsr}$-parameterized system at $g_{Kr} = 0.4$ and $g_{Kr} = 0.38$, respectively. In the $g_{Kr} = 0.4$ case, we superimposed a trajectory (thin gray) and an attractor (cyan) from the

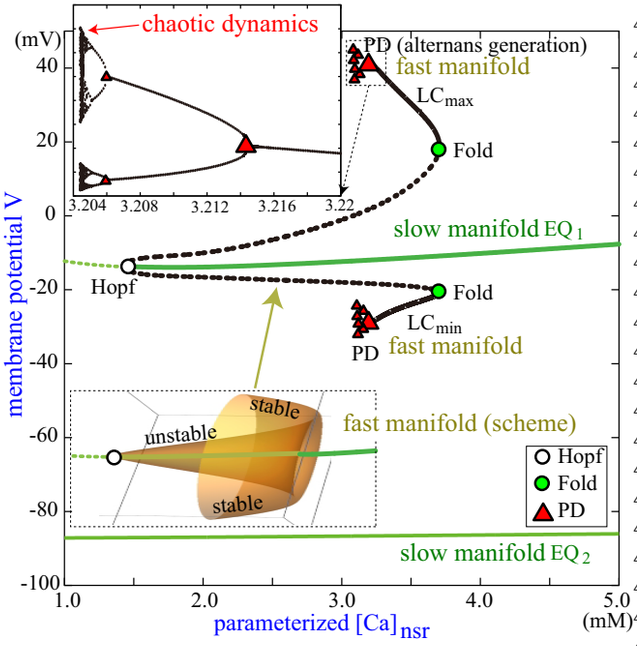

Figure 7. One-parameter bifurcation diagram for $g_{Kr} = 0.38$ (green: equilibrium point (EQ), heavy black curves: limit cycle (LC), solid curves: stable, and dashed curve: unstable) in the $[Ca]_{nsr}$-parameterized system. The maximum and minimum membrane potential of repolarization failure in the original system corresponds to LC_{max} and LC_{min} in the $[Ca]_{nsr}$-parameterized system. The fast-slow decomposition of the parameterized system permits to describe the slow-manifold of equilibria and the fast-manifold of the limit cycles. The fast-manifold has a 'Mexican hat' shape with unstable and stable sheets. The stable branches of limit cycles meet period-doubling bifurcations, leading to a period-doubling cascade into chaotic behavior.

original system. The waveform of this trajectory's membrane potential is shown in Fig. 9. For $g_{Kr} = 0.38$, we superimposed several attractors (cyan, blue, and red).

In Fig. 8(a), the trajectory exhibits ultra-long action potential duration (APD), repolarization failure, transient states with $2-3$ EADs, $1-2$ EADs, 1 EAD, and eventually a normal beat as the steady state. The repolarization failure in the original system corresponds to the stable limit cycle in the $[Ca]_{nsr}$-parameterized system, and the long APD results from the trajectory following the path of the stable equilibrium point in the parameterized system. Additionally, transient EADs are observed between the values of $[Ca]_{nsr}$ associated with the normal and repolarization failure states.

The fast-slow decomposition effectively describes the orbit dynamics, particularly the stable periodic orbit of the normal beat. In this scenario, the orbit remains in quiescence on the slow manifold of equilibrium EQ_2 until a stimulus depolarizes the cell, sending the orbit to the upper branch of the fast-manifold, after which repolarization occurs, restarting the process. As g_{Kr} decreases, these transient EADs become locked into multiple stable EADs, as seen in Fig. 8(b). This is significant because, at lower g_{Kr} values, numerous coexisting patterns with different numbers of EADs appear depending on the initial conditions of the $[Ca]_{nsr}$ variable in the original model. In the parameterized model, there is a multitude of unstable periodic orbits generated by a period-doubling cascade. The presence of such orbits can give rise to multiple coexisting stable periodic orbits if they are stabilized in the original system, as happens at lower g_{Kr} values.

By varying $[Ca]_{nsr}$, we navigate along the fast-manifold of the parameterized model. In Fig. 8(b), we see that on the left side, where $[Ca]_{nsr} \simeq 1.7mM$, the EAD orbit exhibits a 0^m–1 signature, closely resembling the normal beat. However, as $[Ca]_{nsr}$ increases, the stable orbits shift along the fast-manifold, resulting in the emergence of additional EADs generated by the fast loops on the attracting sheets of the manifold. Notably, the normal beat transitions from the slow manifold to the fast-manifold, with EADs being generated on smaller loops within the fast-manifold. In the limiting case, the stable orbit remains entirely on the stable branch of the fast-manifold, without descending to the slow manifold. This condition leads to repolarization failure, as the rapid oscillations inhibit the cell from returning to its original resting state. Fig. 8(b) clearly illustrates this phenomenon, demonstrating how the parameterized study effectively delineates the region of repolarization failure and its bifurcation origins. In this scenario, although the action potential (AP) is present, it fails to fully repolarize the cell. As g_{Kr} increases, stabilized periodic orbits disappear, leaving the normal beat as the only stable state. However, a variety of transient dynamics may still occur due to the presence of unstable periodic orbits, as shown in Fig. 8(a). This combination of using both the original and parameterized systems has provided valuable insights into this high-dimensional problem.

From Figs. 3(b) and 8(b), we observe that higher $[Ca]_{nsr}$ levels promote an increased EAD rate. To illustrate this effect, we present waveforms at $g_{Kr} = 0.36$, where repolarization failure coexists with six distinct EAD types, as shown in Fig. 10. For comparison, we also include a normal state at $g_{Kr} = 0.39$. Additionally, in Fig. 11, we plot the different orbits in a 3D spatial representation of the variables ($[Ca]_{nsr}$, the deactivation gating variable for I_{Ks}, and membrane potential V). This figure highlights the role of fast-slow decomposition: the EADs manifest as rapid rotations on the fast-manifold of the fast subsystem, while the stimulus (applied at the red dot corresponding to the normal beat orbit) compels the orbit to transition from the slow manifold, characterized by quiescent dynamics, to a fast depolarization. We note, as clearly illustrated in Figs. 3(b), 8(b), 10 and 11, that each EAD state is organized by the value of $[Ca]_{nsr}$, since this variable is the slowest in the original system, maintaining a narrow range for each pattern.

V. BASIC CONTROL APPROACH

As demonstrated in previous sections, higher $[Ca]_{nsr}$ levels promote the occurrence of more EADs or small oscillations. Leveraging this characteristic, along with the observation that different patterns are located within narrow ranges of the $[Ca]_{nsr}$ variable, we aimed to control the states by adjust-

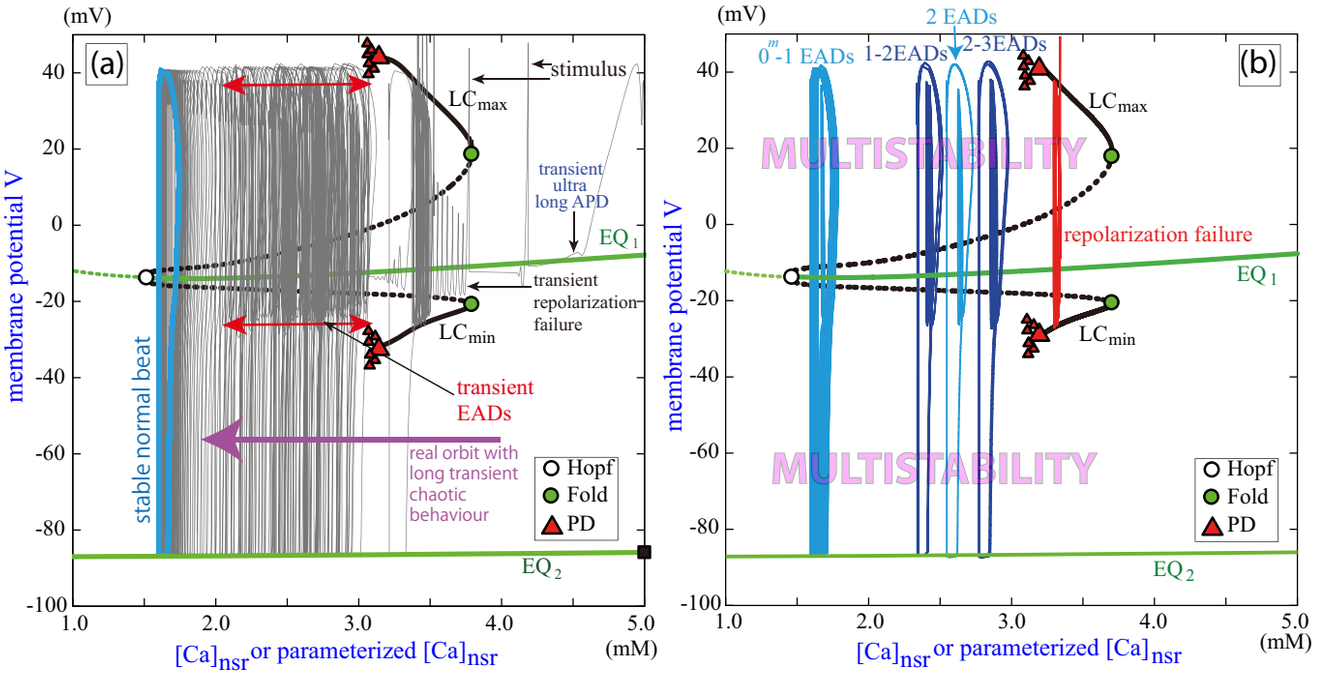

Figure 8. One-parameter bifurcation diagram (green: equilibrium point (EQ), heavy black curves: limit cycle (LC), solid curves: stable, and dashed curve: unstable) in the $[Ca]_{nsr}$-parameterized system. Maximum and minimum membrane potential of repolarization failure in original system corresponds to LC_{max} and LC_{min} in the $[Ca]_{nsr}$-parameterized system. (a) Case $g_{Kr} = 0.4$. Thin gray curve shows a trajectory starting from square point (close to EQ_2 curve) in the original system. Cyan curve represents attractor corresponding to normal state in the original system. This trajectory converges to the attractor orbit via ultra-long APD, repolarization failure, and EADs as transient states. Transient EADs are observed in the region shown by red arrows. (b) Case $g_{Kr} = 0.38$. Blue, cyan and red curves indicate different coexisting attracting orbits in the original system. Stable 0^m–1, 1–2, 2, 2–3 EADs and repolarization failure orbits coexist in the original system. Repolarization failure in the original system corresponds to a stable oscillatory solution in the fast-manifold of the $[Ca]_{nsr}$-parameterized system, leading to persistent EAD oscillations.

ing the value of $[Ca]_{nsr}$ at a single time point.

The results of this straightforward strategy are presented in Fig. 12. Figures 12(a) and 12(b) show the waveforms of the membrane potential, while Figs. 12(c) and 12(d) illustrate the corresponding $[Ca]_{nsr}$ dynamics. The initial states corresponded to the converged values of a 2 EADs state for Figs. 12(a) and 2(c), and to repolarization failure for Figs. 12(b) and 12(d). Notably, we only decreased the value of the $[Ca]_{nsr}$ variable at a single time point, $t = 12500$, within a 37-dimensional system of differential equations. As a result, the membrane potential transitioned to a new stable state, producing fewer EAD states —specifically, a normal state and a $0-1$ EAD state in Figs. 12(a) and 12(b), respectively.

To elucidate the control mechanism, we calculated all the ionic currents following the change in the $[Ca]_{nsr}$ value. Figure 13 displays the membrane potential alongside the ionic current rates, defined as each ionic current divided by the total ionic current. The effects after the $[Ca]_{nsr}$ jump (Figs. 13(b) and 13(d), referred to as "control") are compared with the conditions without the jump (Figs. 13(a) and 13(c), referred to as "no control"). After $t = 12700$, the dominant ionic currents observed are I_{CaL} (Fig. 13(c)) and I_{K1} (Fig. 13(d)). In Fig. 13(c), I_{K1} remains inactive while I_{CaL} becomes predominant after $t = 12800$, leading to the emergence of the EAD, as indicated by the arrow in Fig. 13(a). Conversely, in Fig. 13(d), I_{CaL} is inactive, and I_{K1} becomes active, resulting in the membrane potential returning to the resting state (indicated by the arrow in Fig. 13(b)), thereby preventing the occurrence of EADs.

For a more detailed analysis, we calculated the absolute values of the inward and outward ionic currents. Since $dV/dt = -(I_{ion})$, these values directly influence the rate of change of the membrane potential. Figure 14(a) illustrates the ionic current magnitudes in the vicinity of the decrease in I_{CaL} from Fig. 13(c). The figure indicates that the outward currents (represented by red curves, primarily $I_{Kr}, I_{Ks}, I_{K1}, I_{NaK}$, and I_{Kb}) for both control and no control cases remain nearly identical until $t = 12760$. In contrast, the inward currents (shown by black curves, mainly $I_{NaCa_{ss}}, I_{NaCa_i}$, and I_{CaL}) in the control case peak at $t \simeq 12720$ (highlighted with an ellipse) and subsequently decline due to the reduction in $[Ca]_{nsr}$. In the no control case, the inward and outward currents become equal at $t \simeq 12780$ (marked with a green circle). This crossover signifies a change in the slope of the membrane potential waveform from negative to positive, indicating the onset of EAD.

We also presented the main inward and outward currents during the same time interval in Figs. 14(b) and 14(c), respectively. In Fig. 14(b), I_{CaL} under control conditions shows a

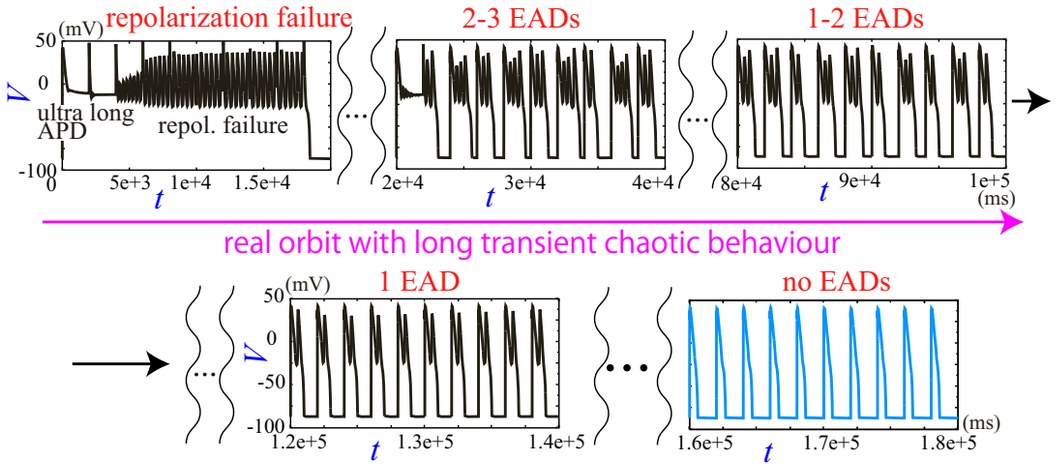

Figure 9. Time series of the membrane potential V in Fig. 8(a) for $g_{Kr} = 0.4$. We observe a transition from repolarization failure to no EADs through several EAD states.

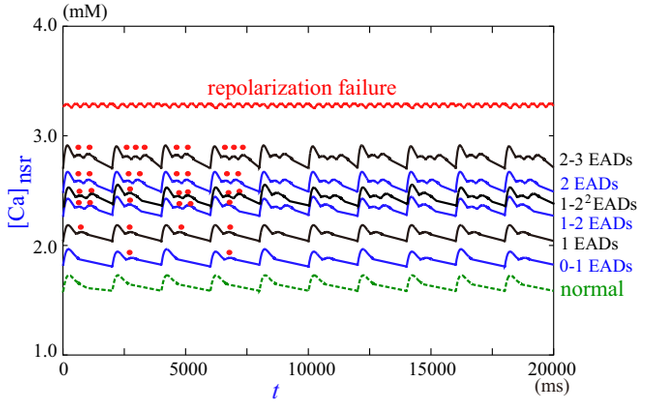

Figure 10. Time series for different initial values of $[Ca]_{nsr}$ at $g_{Kr} = 0.36$. Red dots indicate occurrence of EADs. Normal beat for $g_{Kr} = 0.39$ is shown in dotted green line for comparison.

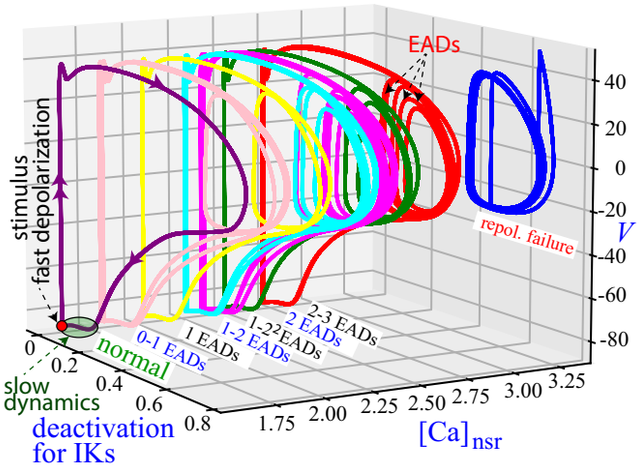

Figure 11. 3D projection ($[Ca]_{nsr}$, the deactivation gating variable for I_{Ks}, membrane potential V) of the different orbits from Fig. 10. The stimulus forces the orbit to leave the slow-manifold, triggering fast depolarization. The EADs are represented as fast rotations on the fast-manifold of the fast subsystem. The different orbits are spatially separated across small $[Ca]_{nsr}$ intervals.

peak at $t \simeq 12720$ (noted with an ellipse), corresponding to the maximum inward current depicted in Fig. 14(a). This peak contributes to the decrease in the membrane potential, which in turn activates the outward current I_{K1}, represented by the dashed magenta curve in Fig. 14(c). Notably, in the control case, I_{K1} is the only outward current that increases significantly. This sharp I_{K1} drives the membrane potential back to its resting state, thus preventing the occurrence of EADs.

Given the limited range for $[Ca]_{nsr}$ (approximately 1 (mM)) and the challenges associated with controlling $[Ca]_{nsr}$ through pharmacological means, we investigated the dependence of $[Ca]_{nsr}$ on pacing cycle length (PCL) and all ionic currents. A decrease in I_{NCX} or an increase in I_{CaL} significantly elevates $[Ca]_{nsr}$ to levels around 2–3 (mM). Interestingly, instead of reducing $[Ca]_{nsr}$ in Fig. 12 (a), increasing I_{NCX} does not eliminate EADs, whereas decreasing I_{CaL} does. A detailed analysis of the underlying mechanisms for this discrepancy will be explored in future work.

VI. DISCUSSION AND CONCLUSION

In this study, we investigated the dependence of early afterdepolarizations (EADs) and repolarization failure on parameter values in O'Hara's realistic mathematical model of human ventricular myocytes. We focused on parameterizing $[Ca]_{nsr}$ (the calcium ion concentration in the network sarcoplasmic reticulum), which is the slowest variable in the system. Through an analysis of bifurcations in the $[Ca]_{nsr}$-parameterized system, we identified the mechanisms underlying the generation of transient states, such as repolarization failure and ultra-long action potential duration (APD) in the original system. Specifically, we demonstrated that the ultra-

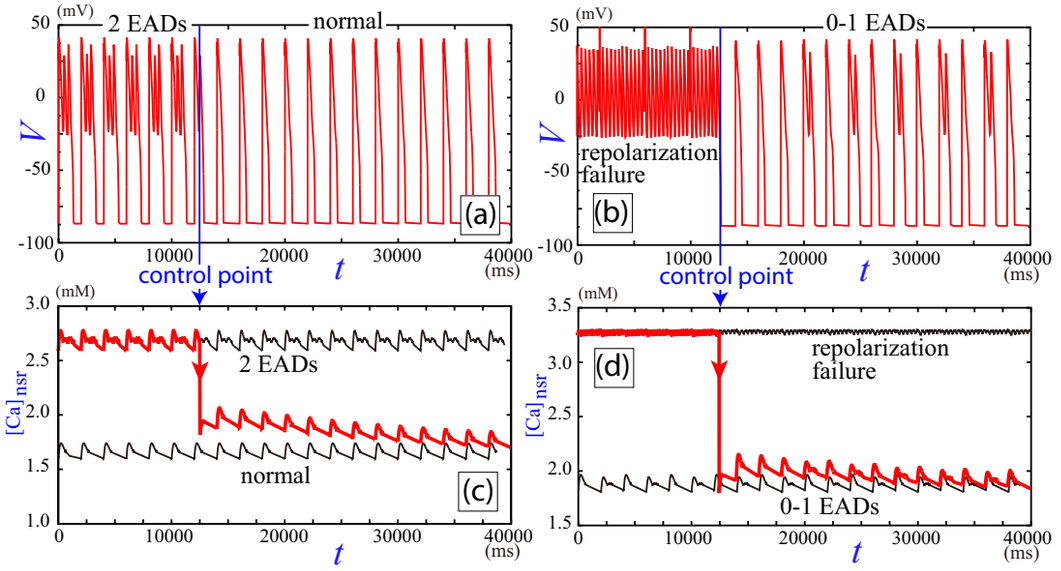

Figure 12. Control of EADs by making slight adjustments to the value of $[Ca]_{nsr}$ at a single time point. Values of $[Ca]_{nsr}$ are changed at $t = 12500$ ms for $g_{Kr} = 0.39$ ((a) and (c)) and $g_{Kr} = 0.36$ ((b) and (d)). (a) Time series of the membrane potential V transitioning from 2 EADs to normal. (b) Time series of the membrane potential transitioning from repolarization failure to 0–1 EADs. (c) Time series of the $[Ca]_{nsr}$ variable. Upper and lower black curves indicate $[Ca]_{nsr}$ for 2 EADs and normal, respectively. (d) Time series of the $[Ca]_{nsr}$ variable. Upper and lower black curves indicate $[Ca]_{nsr}$ for repolarization failure and 0–1 EADs, respectively.

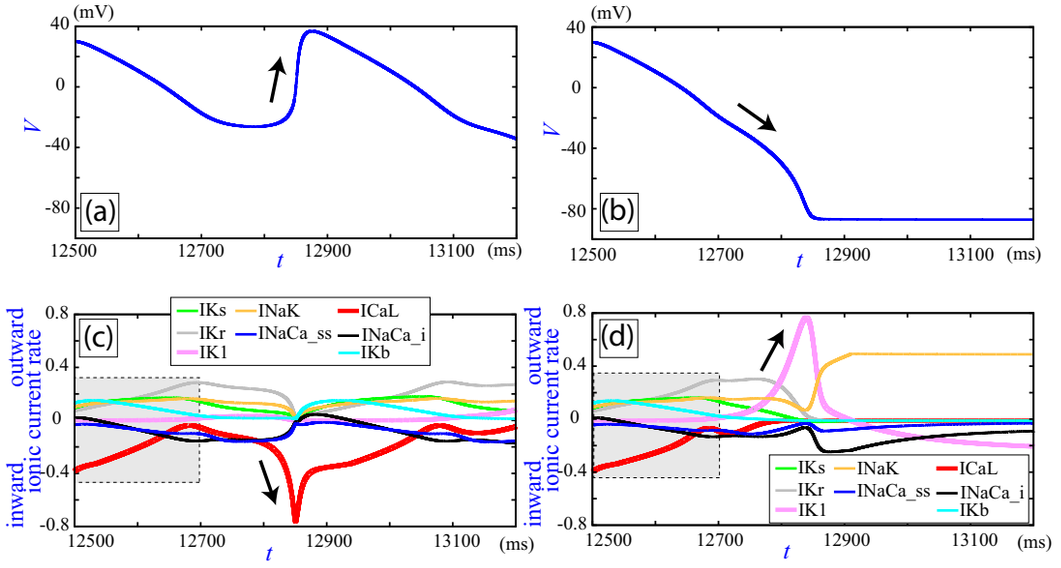

Figure 13. Membrane potential and main ionic current rates (> 10% at most) after a jump in $[Ca]_{nsr}$ (control) and without a jump (no control) at $g_{Kr} = 0.39$. Ionic current rates are almost the same for both cases in the gray region. (a) Membrane potential with EAD (no control). (b) Normal membrane potential (control). (c) Ionic current rate (no control). (d) Ionic current rate (control).

long APD observed in the original model is due to a trajectory that follows the locus of a stable equilibrium point in the $[Ca]_{nsr}$-parameterized system. Higher values of $[Ca]_{nsr}$ lead to longer APDs. Moreover, using the parameterized model enabled a fast-slow decomposition of the original system, providing a dynamical systems perspective on the diverse behaviors observed. In particular, it revealed that the repolarization failure state corresponds to a stable branch of the limit cycles (fast-manifold) in the $[Ca]_{nsr}$-parameterized system. Additionally, the EADs were shown to follow the fast-manifold of this parameterized system. The bifurcation analysis also highlighted the critical role of alternans formation (via period-doubling bifurcations in this case) in generating an infinite number of unstable periodic orbits through a period-doubling

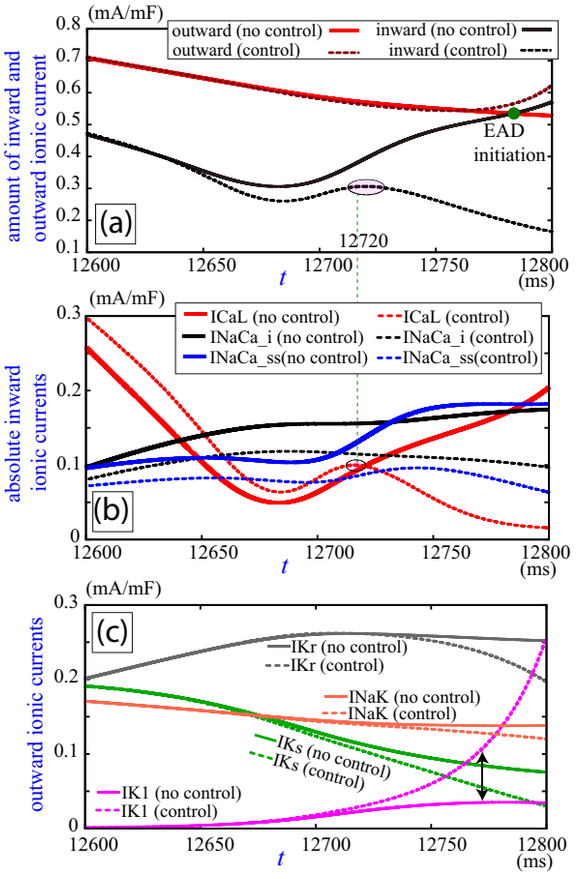

Figure 14. Ionic currents near the activation of I_{CaL} and I_{K1}, as shown in Fig. 13. (a) Total inward and outward ionic currents with and without control. (b) Main inward ionic currents (absolute value) with and without control in the same interval as (a). (c) Main outward ionic currents with and without control in the same interval as (a).

cascade. This instability permits transient chaotic dynamics and the stabilization of multiple coexisting EAD states.

It is important to note that other slow variables, such as the slow accumulation of [Na] or the slow recovery of I_{Ks}, may also contribute to the complex dynamics of EADs. Given the limited range of $[Ca]_{nsr}$, these additional slow variables likely play a significant role, and exploring their influence will be part of our future research.

We discovered numerous coexisting states, such as EADs, repolarization failure, and normal beats, which were categorized based on the value of $[Ca]_{nsr}$. Leveraging this property, we proposed a method for controlling these states. By simply decreasing the value of $[Ca]_{nsr}$ in a 37-dimensional system of differential equations, we were able to transform EAD or repolarization failure behavior into a normal state. Our results indicate that this transformation occurs as follows: a reduction in $[Ca]_{nsr}$ also lowers calcium concentrations in the subspace, junctional SR, and myoplasmic compartments. These reductions inhibit Na/Ca exchanger activity, as described in Ref. 53, leading to a decrease in Na/Ca exchange currents ($I_{NaCa_{ss}}$ and I_{NaCa_i}). This, in turn, causes inactivation of the L-type calcium channels, resulting in a decrease in membrane potential. The lowered membrane potential then activates I_{K1}, further reducing the potential to the resting state, thereby eliminating the EAD and restoring the normal rhythm.

Previous studies[40,54] have categorized EADs into two types: (1) secondary activation of the L-type calcium current during the plateau phase of the action potential, and (2) activation of the Na/Ca exchange current due to increased the calcium ion concentration in the myoplasmic compartment, following spontaneous calcium release from the SR during the late repolarization phase. Our research focused on EAD generation corresponding to type (1), while inhibiting EADs using the opposite mechanism described in type (2). We confirmed that lowering the calcium ion concentration in various compartments (junctional SR, subspace, and myoplasmic compartments) also suppressed EAD generation. However, this reduction in $[Ca]_{nsr}$ further decreased membrane potential, ultimately determining whether the system stabilized in an EAD state or returned to normal. Investigating EAD generation under type (2) conditions and examining the effects of lowering $[Ca]_{nsr}$ in other mathematical models remain open areas of research. Additionally, understanding the relationship between calcium ion concentrations and delayed afterdepolarizations will be a key focus in future studies.

Our study has some limitations. First, while we found evidence suggesting a role for $[Ca]_{nsr}$ in EAD generation, it remains challenging to control $[Ca]_{nsr}$ precisely in experiments. Spencer et al.[45] reported that action potential prolongation was sensitive to inhibition of Na/Ca exchange in experimental settings. Since inhibiting Na/Ca exchange elevates $[Ca]_{nsr}$, this suggests that the fundamental mechanism may be related to an increase in $[Ca]_{nsr}$. Second, our investigation was limited to a single mathematical model. Further studies using additional models are necessary to confirm the role of $[Ca]_{nsr}$ in EAD generation. All these open questions will be addressed in our upcoming research.

ACKNOWLEDGMENTS

We thank Prof. T. Yoshinaga of Tokushima University for providing his powerful bifurcation analysis tools. This research was supported by JST Moonshot R&D Grant Number JPMJMS2021. RB has been supported by the Agencia Estatal de Investigación (Spain) and European Regional Development Fund (project PID2021-122961NB-I00), Diputación General de Aragón and European Regional Development Fund (project E24-23R) and Agencia Estatal de Investigación (Spain) (project TED2021-130459B-I00).

AUTHOR DECLARATIONS

CONFLICT OF INTEREST

The authors have no conflicts to disclose.

AUTHOR CONTRIBUTIONS

Hiroyuki Kitajima: Funding acquisition (equal); Formal analysis (lead); Software (lead); Investigation (lead); Methodology (equal); Writing-original draft (lead); Writing-review & editing (equal). Toru Yazawa: Formal analysis (supporting); Investigation (supporting); Methodology (supporting). Roberto Barrio: Funding acquisition (equal); Writing-review & editing (equal); Methodology (equal); Visualization (lead); Investigation (supporting).

DATA AVAILABILITY STATEMENT

The data that support the findings of this study are available within the article.

REFERENCES

[1]B.-R. Choi, F. Burton, and G. Salama, "Cytosolic Ca2+ triggers early afterdepolarizations and Torsade de Pointes in rabbit hearts with type 2 long QT syndrome," The Journal of physiology **543**, 615–631 (2002).

[2]P. G. Volders, M. A. Vos, B. Szabo, K. R. Sipido, S. M. de Groot, A. P. Gorgels, H. J. Wellens, and R. Lazzara, "Progress in the understanding of cardiac early afterdepolarizations and Torsades de Pointes: time to revise current concepts," Cardiovascular research **46**, 376–392 (2000).

[3]Y. Tsuji, M. Yamazaki, M. Shimojo, S. Yanagisawa, Y. Inden, and T. Murohara, "Mechanisms of torsades de pointes: an update," Frontiers in Cardiovascular Medicine **11** (2024), 10.3389/fcvm.2024.1363848.

[4]S. Zimik, N. Vandersickel, A. R. Nayak, A. V. Panfilov, and R. Pandit, "A comparative study of early afterdepolarization-mediated fibrillation in two mathematical models for human ventricular cells," PloS one **10**, e0130632 (2015).

[5]Z. Zhao, Y. Xie, H. Wen, D. Xiao, C. Allen, N. Fefelova, W. Dun, P. A. Boyden, Z. Qu, and L.-H. Xie, "Role of the transient outward potassium current in the genesis of early afterdepolarizations in cardiac cells," Cardiovascular research **95**, 308–316 (2012).

[6]J. Zeng and Y. Rudy, "Early afterdepolarizations in cardiac myocytes: mechanism and rate dependence," Biophysical journal **68**, 949–964 (1995).

[7]J. N. Weiss, A. Garfinkel, H. S. Karagueuzian, P.-S. Chen, and Z. Qu, "Early afterdepolarizations and cardiac arrhythmias," Heart rhythm **7**, 1891–1899 (2010).

[8]Z. Qu, L.-H. Xie, R. Olcese, H. S. Karagueuzian, P.-S. Chen, A. Garfinkel, and J. N. Weiss, "Early afterdepolarizations in cardiac myocytes: beyond reduced repolarization reserve," Cardiovascular research **99**, 6–15 (2013).

[9]P. C. Viswanathan and Y. Rudy, "Pause induced early afterdepolarizations in the long QT syndrome: a simulation study," Cardiovascular research **42**, 530–542 (1999).

[10]N. Vandersickel, I. V. Kazbanov, A. Nuitermans, L. D. Weise, R. Pandit, and A. V. Panfilov, "A study of early afterdepolarizations in a model for human ventricular tissue," PloS one **9**, e84595 (2014).

[11]C. T. January and J. M. Riddle, "Early afterdepolarizations: mechanism of induction and block. A role for L-type Ca2+ current." Circulation research **64**, 977–990 (1989).

[12]K. Furutani, K. Tsumoto, I.-S. Chen, K. Handa, Y. Yamakawa, J. T. Sack, and Y. Kurachi, "Facilitation of I Kr current by some hERG channel blockers suppresses early afterdepolarizations," Journal of General Physiology **151**, 214–230 (2019).

[13]X. Huang, Z. Song, and Z. Qu, "Determinants of early afterdepolarization properties in ventricular myocyte models," PLoS computational biology **14**, e1006382 (2018).

[14]C. O. Diekman and N. Wei, "Circadian rhythms of early afterdepolarizations and ventricular arrhythmias in a cardiomyocyte model," Biophysical Journal **120**, 319–333 (2021).

[15]Y. Kurata, K. Tsumoto, K. Hayashi, I. Hisatome, M. Tanida, Y. Kuda, and T. Shibamoto, "Dynamical mechanisms of phase-2 early afterdepolarizations in human ventricular myocytes: insights from bifurcation analyses of two mathematical models," American Journal of Physiology-Heart and Circulatory Physiology **312**, H106–H127 (2017).

[16]S. Sridhar, N. Vandersickel, and A. V. Panfilov, "Effect of myocyte-fibroblast coupling on the onset of pathological dynamics in a model of ventricular tissue," Scientific reports **7**, 40985 (2017).

[17]Z. Zhang and Z. Qu, "Mechanisms of phase-3 early afterdepolarizations and triggered activities in ventricular myocyte models," Physiological Reports **9**, e14883 (2021).

[18]Y. Xie, L. T. Izu, D. M. Bers, and D. Sato, "Arrhythmogenic transient dynamics in cardiac myocytes," Biophysical Journal **106**, 1391–1397 (2014).

[19]R. Barrio, M. A. Martínez, L. Pérez, and E. Pueyo, "Bifurcations and slow-fast analysis in a cardiac cell model for investigation of early afterdepolarizations," Mathematics **8**, 880 (2020).

[20]E. Slepukhina, L. Ryashko, and P. Kügler, "Noise-induced early afterdepolarizations in a three-dimensional cardiac action potential model," Chaos, Solitons & Fractals **131**, 109515 (2020).

[21]Z. Chu, D. Yang, and X. Huang, "Conditions for the genesis of early afterdepolarization in a model of a ventricular myocyte," Chaos: An Interdisciplinary Journal of Nonlinear Science **30** (2020).

[22]D. X. Tran, D. Sato, A. Yochelis, J. N. Weiss, A. Garfinkel, and Z. Qu, "Bifurcation and chaos in a model of cardiac early afterdepolarizations," Physical review letters **102**, 258103 (2009).

[23]M. G. Chang, C. Y. Chang, E. De Lange, L. Xu, B. O'Rourke, H. S. Karagueuzian, L. Tung, E. Marbán, A. Garfinkel, J. N. Weiss, *et al.*, "Dynamics of early afterdepolarization-mediated triggered activity in cardiac monolayers," Biophysical journal **102**, 2706–2714 (2012).

[24]P. Kügler, A. H. Erhardt, and M. Bulelzai, "Early afterdepolarizations in cardiac action potentials as mixed mode oscillations due to a folded node singularity," PLoS One **13**, e0209498 (2018).

[25]T. Vo and R. Bertram, "Why pacing frequency affects the production of early afterdepolarizations in cardiomyocytes: An explanation revealed by slow-fast analysis of a minimal model," Physical Review E **99**, 052205 (2019).

[26]A. H. Erhardt, "Early afterdepolarisations induced by an enhancement in the calcium current," Processes **7**, 20 (2019).

[27]J. Kimrey, T. Vo, and R. Bertram, "Big ducks in the heart: Canard analysis can explain large early afterdepolarizations in cardiomyocytes," SIAM Journal on Applied Dynamical Systems **19**, 1701–1735 (2020).

[28]R. Barrio, J. A. Jover-Galtier, M. Martínez, L. Pérez, and S. Serrano, "Mathematical birth of early afterdepolarizations in a cardiomyocyte model," Mathematical Biosciences **366**, 109088 (2023).

[29]P. Kügler, M. Bulelzai, and A. H. Erhardt, "Period doubling cascades of limit cycles in cardiac action potential models as precursors to chaotic early afterdepolarizations," BMC Systems Biology **11**, 1–13 (2017).

[30]P. Kügler, "Early afterdepolarizations with growing amplitudes via delayed subcritical hopf bifurcations and unstable manifolds of saddle foci in cardiac action potential dynamics," PLoS One **11**, e0151178 (2016).

[31]J. Landaw and Z. Qu, "Bifurcations caused by feedback between voltage and intracellular ion concentrations in ventricular myocytes," Physical review letters **123**, 218101 (2019).

[32]T. Krogh-Madsen and D. J. Christini, "Slow [Na+] i dynamics impacts arrhythmogenesis and spiral wave reentry in cardiac myocyte ionic model," Chaos: An Interdisciplinary Journal of Nonlinear Science **27** (2017).

[33]K. Tsumoto, Y. Kurata, K. Furutani, and Y. Kurachi, "Hysteretic dynamics of multi-stable early afterdepolarisations with repolarisation reserve attenuation: a potential dynamical mechanism for cardiac arrhythmias," Scientific reports **7**, 10771 (2017).

[34]Y. Xie, Z. Liao, E. Grandi, Y. Shiferaw, and D. M. Bers, "Slow [Na] i changes and positive feedback between membrane potential and [Ca] i underlie intermittent early afterdepolarizations and arrhythmias," Circulation: Arrhythmia and Electrophysiology **8**, 1472–1480 (2015).

[35]H. Kitajima and T. Yazawa, "Bifurcation analysis on a generation of early afterdepolarization in a mathematical cardiac model," International Journal of Bifurcation and Chaos **31**, 2150179 (2021).

[36]T. J. Hund, J. P. Kucera, N. F. Otani, and Y. Rudy, "Ionic charge conservation and long-term steady state in the Luo–Rudy dynamic cell model," Biophysical journal **81**, 3324–3331 (2001).

[37]M. Fink, P. J. Noble, and D. Noble, "Ca2+-induced delayed afterdepolarizations are triggered by dyadic subspace Ca2+ affirming that increasing SERCA reduces aftercontractions," American Journal of Physiology-Heart and Circulatory Physiology **301**, H921–H935 (2011).

[38]Y. Kurata, K. Tsumoto, K. Hayashi, I. Hisatome, Y. Kuda, and M. Tanida, "Multiple dynamical mechanisms of phase-2 early afterdepolarizations in a human ventricular myocyte model: Involvement of spontaneous SR Ca 2+ release," Frontiers in Physiology **10**, 1545 (2020).

[39]Z. Song, C. Y. Ko, M. Nivala, J. N. Weiss, and Z. Qu, "Calcium-voltage coupling in the genesis of early and delayed afterdepolarizations in cardiac myocytes," Biophysical journal **108**, 1908–1921 (2015).

[40]C.-H. Luo and Y. Rudy, "A dynamic model of the cardiac ventricular action potential. II. Afterdepolarizations, triggered activity, and potentiation." Circulation research **74**, 1097–1113 (1994).

[41]R. Barrio, M. Martínez, E. Pueyo, and S. Serrano, "Dynamical analysis of early afterdepolarization patterns in a biophysically detailed cardiac model," Chaos: An Interdisciplinary Journal of Nonlinear Science **31** (2021).

[42]R. Barrio, M. Á. Martínez, S. Serrano, and E. Pueyo, "Dynamical mechanism for generation of arrhythmogenic early afterdepolarizations in cardiac myocytes: Insights from in silico electrophysiological models," Physical Review E **106**, 024402 (2022).

[43]M. M. Adamantidis, P. Kerram, J. F. Caron, and B. Dupuis, "Droperidol exerts dual effects on repolarization and induces early afterdepolarizations and triggered activity in rabbit Purkinje fibers." Journal of Pharmacology and Experimental Therapeutics **266**, 884–893 (1993).

[44]F. L. Puisieux, M. M. Adamantidis, B. M. Dumotier, and B. A. Dupuis, "Cisapride-induced prolongation of cardiac action potential and early afterdepolarizations in rabbit Purkinje fibres," British journal of pharmacology **117**, 1377–1379 (1996).

[45]C. I. Spencer, S. Baba, K. Nakamura, E. A. Hua, M. A. Sears, C.-c. Fu, J. Zhang, S. Balijepalli, K. Tomoda, Y. Hayashi, *et al.*, "Calcium transients closely reflect prolonged action potentials in iPSC models of inherited cardiac arrhythmia," Stem cell reports **3**, 269–281 (2014).

[46]N. El-Sherif, R. H. Zeiler, W. Craelius, W. B. Gough, and R. Henkin, "QTU prolongation and polymorphic ventricular tachyarrhythmias due to bradycardia-dependent early afterdepolarizations. Afterdepolarizations and ventricular arrhythmias." Circulation research **63**, 286–305 (1988).

[47]C. Cang, K. Aranda, and D. Ren, "A non-inactivating high-voltage-activated two-pore Na+ channel that supports ultra-long action potentials and membrane bistability," Nature communications **5**, 5015 (2014).

[48]Z. Qu and D. Chung, "Mechanisms and determinants of ultralong action potential duration and slow rate-dependence in cardiac myocytes," PLoS One **7** (2012).

[49]S. Heitmann, A. Shpak, J. I. Vandenberg, and A. P. Hill, "Arrhythmogenic effects of ultra-long and bistable cardiac action potentials," PLOS Computational Biology **17**, e1008683 (2021).

[50]T. O'Hara, L. Virág, A. Varró, and Y. Rudy, "Simulation of the undiseased human cardiac ventricular action potential: model formulation and experimental validation," PLoS computational biology **7**, e1002061 (2011).

[51]H. Kawakami, "Bifurcation of periodic responses in forced dynamic nonlinear circuits: Computation of bifurcation values of the system parameters," IEEE Transactions on circuits and systems **31**, 248–260 (1984).

[52]D. D. Chen, R. A. Gray, I. Uzelac, C. Herndon, and F. H. Fenton, "Mechanism for amplitude alternans in electrocardiograms and the initiation of spatiotemporal chaos," Phys. Rev. Lett. **118**, 168101 (2017).

[53]Y. Kurata, I. Hisatome, and T. Shibamoto, "Roles of sarcoplasmic reticulum Ca2+ cycling and Na+/Ca2+ exchanger in sinoatrial node pacemaking: insights from bifurcation analysis of mathematical models," American Journal of Physiology-Heart and Circulatory Physiology **302**, H2285–H2300 (2012).

[54]Z. Zhao, H. Wen, N. Fefelova, C. Allen, A. Baba, T. Matsuda, and L.-H. Xie, "Revisiting the ionic mechanisms of early afterdepolarizations in cardiomyocytes: predominant by Ca waves or Ca currents?" American Journal of Physiology-Heart and Circulatory Physiology **302**, H1636–H1644 (2012).